Hyperfine couplings as a probe of orbital anisotropy in heavy-fermion materials

P. Menegasso,[1] J. C. Souza,[1] I. Vinograd,[2] Z. Wang,[2] S. P. Edwards,[2] P. G. Pagliuso,[1] N. J. Curro,[2] and R. R. Urbano[1]
[1]*Instituto de Física "Gleb Wataghin," UNICAMP, Campinas, São Paulo 13083-859, Brazil*
[2]*Department of Physics, University of California, Davis, California 95616, USA*

(Received 25 November 2020; revised 30 April 2021; accepted 7 July 2021; published 27 July 2021)

Overlap between neighboring atomic wave functions is a central feature of conducting solids. In heavy-fermion materials, f-electron orbitals in the lattice lie on the boundary between fully localized and hybridized in an energy band. This dichotomy gives rise to a range of behaviors, including antiferromagnetism, unconventional superconductivity, and the ability to tune from one ground state to the other continuously. Measuring the degree of this hybridization by traditional methods is challenging and indirect. We utilize an approach using NMR to determine the magnetic couplings between the f electrons and neighboring nuclear spins in a series of $CeRh_{1-x}Ir_xIn_5$ crystals and find that the hybridization is strongly direction dependent in this important class of superconducting heavy-fermion materials. Our results demonstrate that hyperfine coupling measurements provide a quantitative measure of orbital anisotropy.

DOI: 10.1103/PhysRevB.104.035154

I. INTRODUCTION

Heavy-fermion metals are characterized by strong electron-electron interactions that can be tuned across a quantum phase transition between localized f-electron magnetism and itinerant heavy-mass Fermi liquid behavior [1–3]. The crossover between these two extremes is controlled by the degree to which the f-electron orbitals hybridize with neighboring atoms to form dispersive bands [4–7]. Theoretical models typically assume that variables such as pressure or doping ("chemical pressure") indirectly modify the small wave function overlap between the Ce $4f$ electrons and itinerant conduction electron bands, which consequently alter the low-energy degrees of freedom [8–11]. Detailed information about this hybridization has required complex quantum chemistry calculations [12] or indirect analysis of experiments [13–15].

The tetragonal $CeMIn_5$ (M = Co, Rh, Ir) materials (see Fig. 1) are prototypical heavy-fermion systems, exhibiting quantum criticality, antiferromagnetism, and unconventional superconductivity across a phase diagram that can be tuned with pressure, magnetic field, or substitution at the transition metal site [16–19]. One of the outstanding mysteries in these materials is how the transition metal M changes the $4f$ hybridization and hence the ground state. Similar physics is at play in the actinide $PuMGa_5$ (M = Co, Rh) materials, where the superconducting transition temperature is an order of magnitude larger [20–22]. For parts of the phase diagram where the ground state is superconducting, T_c appears to correlate with the lattice anisotropy at ambient pressure [23,24]. However, this relationship breaks down when the ground state evolves towards antiferromagnetism.

Recently, an x-ray absorption spectroscopy (XAS) study probed the nature of the Ce $4f$ crystalline electrical field (CEF) ground state wave functions for several different $CeRh_xIr_{1-x}In_5$ crystals [14]. These studies revealed a change in the shape of the wave function, lending support to the idea that the hybridization of the $4f$ electrons is strongly momentum dependent [12,13]. Electronic structure calculations indicated that the momentum dependence affects the hybridization with the in-plane In(1) and out-of-plane In(2) $5p$ electrons differently, leading to multiple hybridization gaps at low temperature. Surprisingly, the In(2) electrons appear to be more strongly coupled to the $4f$ moments, suggesting that substitution at the M site may affect this coupling and hence the nature of the ground state.

In order to investigate the nature of this hybridization in more detail, we have measured the nuclear magnetic resonance (NMR) Knight shift in $CeRh_xIr_{1-x}In_5$ for both In(1) and In(2) sites. The In nuclear spins ($I = 9/2$) experience a transferred hyperfine field that reflects the hybridization to the $4f$ electrons [25,26]. The hyperfine coupling between a nuclear spin $\mathbf{I}$ at $\mathbf{r} = 0$ and an electronic spin at $\mathbf{r}$ is given by

$$\mathcal{H}_{hyp} = g\mu_B\gamma\hbar\mathbf{I}\cdot\left(\frac{8\pi}{3}\delta(\mathbf{r})\mathbf{S} + 3\frac{\mathbf{r}(\mathbf{S}\cdot\mathbf{r})}{r^5} - \frac{\mathbf{S}}{r^3}\right), \quad (1)$$

where γ is the nuclear gyromagnetic ratio and μ_B is the Bohr magneton. The first term is the Fermi contact term relevant for s orbitals, and the second and third terms constitute a dipolar interaction with the electron spin. Typically, both contact and dipolar terms are present, as well as multiple electron spins, leading to an effective hyperfine coupling tensor that in practice is determined empirically and contains both Fermi-contact and dipolar components. Often, the magnitude of the dipolar component exceeds the direct dipolar field for a localized spin by at least an order of magnitude, e.g., in this case the dipolar field of a moment located at the origin of the Ce atom. This enhancement is due to hybridization of the orbitals of the unpaired electron spin with the relevant orbitals surrounding

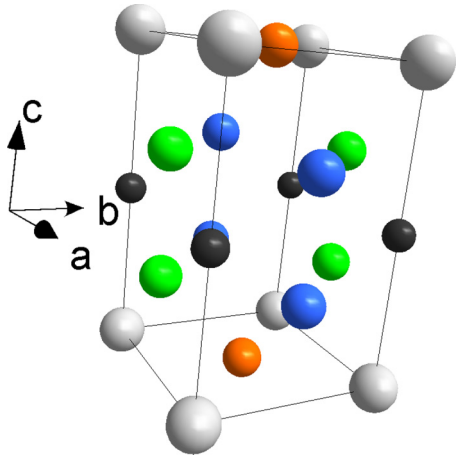

FIG. 1. Crystal structure of the $CeMIn_5$ system. Gray corresponds to the Ce sites, orange corresponds to In(1), green and blue correspond to In(2), and black corresponds to the M site. Note that $a = b$ in this tetragonal system, but the In(2) sites exhibit different Knight shifts for field along a versus b.

the nucleus. These so-called *transferred* hyperfine couplings depend sensitively on the electronic wave function [27].

In heavy fermions, there are two sets of electronic spins: those associated with the itinerant conduction electrons, $\mathbf{S}_c$, and with the $4f$ orbitals, $\mathbf{S}_f$. There are different hyperfine coupling tensors to these two degrees of freedom: $\mathcal{H}_{hyp} = g\mu_B\gamma\hbar\mathbf{I}\cdot[\mathbb{A}\cdot\mathbf{S}_c + \sum_i \mathbb{B}_i\cdot\mathbf{S}_f(\mathbf{r}_i)]$, where $\mathbb{A}$ corresponds to an on-site coupling to the conduction electron spins [28] and $\mathbb{B}_i$ are the transferred couplings to the nearest-neighbor $4f$ spins. The transferred couplings can be determined by comparing the Knight shift and bulk susceptibility as a function of temperature and field direction and have been well documented for the stoichiometric $CeMIn_5$ materials [15,28–30]. Surprisingly, the transferred coupling $B_{cc}(1)$ for the In(1) site decreases by a factor of 3 between M = Rh and M = Co, whereas $B_{cc}(2)$ for the In(2) site increases by the same factor. A similar evolution of $B_{cc}(1)$ has been observed in $CeRhIn_5$ under modest hydrostatic pressure as the ground state evolves from antiferromagnetic to superconducting [31]. Such a large variability in transferred hyperfine couplings constants has not been observed in other strongly correlated superconductors, such as the cuprates, iron pnictides, or chalcogenides. We posit that in the $CeMIn_5$ materials the transferred hyperfine couplings arises due to the hybridization between the Ce $4f$ ground state orbital and the In $5p$ states and that the variations in the coupling constant reflect changes in the shape of the ground state $4f$ orbital.

II. METHODS

High-quality single crystals of $CeRh_xIr_{1-x}In_5$ with multiple values of x were grown via the flux method technique [32,33]. Single crystals of tetragonal shape were selected manually and polished to remove In flux from the surface. Powder x-ray diffraction measurements in a Bruker Phaser D2 diffractometer with Cu $K\alpha$ radiation ($\lambda = 1.5418$ Å) using a silicon plate with zero background confirmed the expected tetragonal phase without evidence of spurious phases.

Magnetic susceptibility experiments were carried out on a commercial Quantum Design PPMS-14T, with an insert for vibrating-sample magnetometer magnetization measurements in the range $3 < T < 300$ K, in a magnetic field of 8 T. NMR experiments were carried out in a high-homogeneity fixed-field magnet with field $H_0 = 11.7294$ T for a range of temperatures down to 5 K. Samples were mounted with $\mathbf{H}_0 \,||\, c$, and radio frequency pulses of varying duration (1.9–2.2 μs) were used. Spectra at multiple frequencies were acquired and summed over a broad range to identify multiple satellites of each In site.

III. RESULTS

A. Magnetic susceptibility

Figure 2 shows the bulk magnetic susceptibility χ of a series of single crystals of $CeRh_{1-x}Ir_xIn_5$ between 4 and 300 K. χ varies strongly between 4 and 300 K, reflecting the localized nature of the Ce $4f$ electrons. For $T > 50$ K, χ is well described by local moments in a tetragonal crystal field, with an effective exchange interaction, as discussed in [34]. This behavior is modified at low temperature due to the crystal field splitting, the Kondo interaction, and the exchange interaction among the Ce orbitals, all of which depend on the doping x. As x increases, the ground state evolves from antiferromagnetic below the Néel temperature $T_N = 3.8$ K ($x = 0$) to superconducting below $T_c = 0.4$ K ($x = 1$), with a possible quantum phase transition near $x = 0.3$ [35]. de Haas–van Alphen measurements and band structure calculations indicate that the $4f$ electrons become more itinerant, and this trend is reflected in the overall decrease in the magnitude of χ over this range [36,37].

The behavior of an isolated Ce $4f$ electron spin in a tetragonal environment is given by $\mathcal{H}_{CEF} = B_2^0\hat{O}_2^0 + B_4^0\hat{O}_4^0 + B_4^4\hat{O}_4^4$, where $\hat{O}_n^m$ are the Stevens operators and B_n^m are parameters that characterize the crystal field. The $J = 5/2$ multiplet is split into three Kramers doublets: $\Gamma_7^{(1)}$, $\Gamma_7^{(2)}$, and Γ_6. The

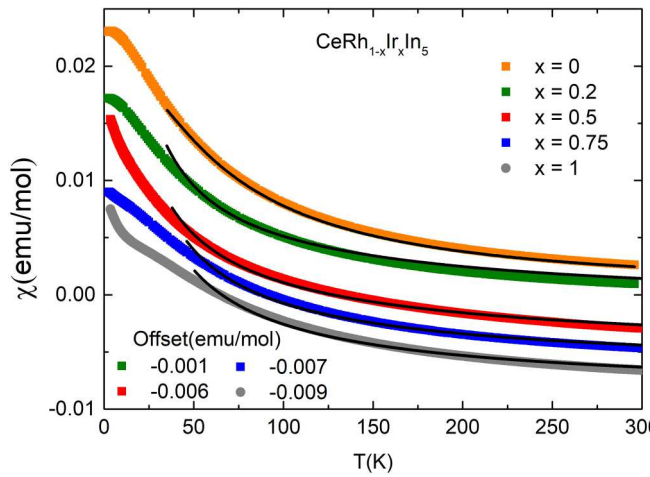

FIG. 2. Bulk susceptibility along the c axis of $CeRh_{1-x}Ir_xIn_5$ versus temperature. The solid lines are fits to the high-temperature data, as described in the text. The curves have been offset vertically for clarity with values of −0.001, −0.006, −0.007, and −0.009 emu/mol for $x = 0.2$, 0.5, 0.75, and 1, respectively.

TABLE I. EFG, hyperfine, and CEF parameters for $CeRh_{1-x}Ir_xIn_5$ and $CeCoIn_5$. Values for $x = 0$, $x = 1$, and $CeCoIn_5$ are reproduced from [28,29,39]. Hyperfine couplings are given in units of kOe/μ_B.

x	$\nu_{zz}(1)$ (MHz)	$\nu_{zz}(2)$ (MHz)	$\eta(2)$	$B_{cc}(1)$	$B_{cc}(2)$	B_2^0 (meV)	B_4^0 (meV)	$\lvert B_4^4\rvert$ (meV)	α^2
0	6.78	16.665	0.445	21.4	4.1	−0.928	0.052	0.128	0.407
0.20	6.4(5)	17.3(8)	0.45	20.0(2.0)		−0.961	0.057	0.118	0.37
0.50	6.3(5)	16.5(8)	0.45	16.7(4)		−0.996	0.061	0.107	0.28
0.75	6.0(5)	17.3(8)	0.45	15.0(4.0)		−1.154	0.068	0.86	0.26
1	6.07	18.17	0.46	13.8	15.9	−1.197	0.069	0.088	0.250
$CeCoIn_5$	8.173	15.489	0.386	8.9	28.1	−0.856	0.063	0.089	0.129

ground state $\Gamma_7^{(1)}$ wave functions can be expressed as

$$|\psi(\Gamma_7^{(1)})\rangle = \alpha\left|\pm\frac{5}{2}\right\rangle + \sqrt{1-\alpha^2}\left|\mp\frac{3}{2}\right\rangle, \tag{2}$$

where α characterizes the degree of mixing between the J_z manifolds and controls the degree of spatial anisotropy of the orbital. $\alpha_c^2 = 1/6$ for cubic symmetry ($B_4^4 = 4B_4^0$ and $B_2^0 = 0$). α^2 increases as the CEF potential becomes more tetragonal and the orbital shape becomes more two-dimensional.

The magnetic susceptibility of the f moments is given by $\chi_{ff}^{-1} = \chi_{ff0}^{-1} + \lambda$, where λ is a mean-field parameter that captures both the exchange and Kondo interactions [34] and χ_{ff0} is determined by the local moments in $\mathcal{H}_{CEF}$, as described in [38]. We assume that the f moments dominate the magnetic response and fit the susceptibility data for $T > 50$ K to extract the fitting parameters B_2^0, B_4^0, B_4^4, and λ, as detailed in Table I. The α^2 values are determined by the eigenvectors of $\mathcal{H}_{CEF}$ with these fit parameters. Although fitting the susceptibility data is an indirect and less precise approach to extracting the CEF parameters than direct XAS measurements, our values agree well with published results [14].

B. NMR spectra

Figure 3 shows ^{115}In NMR spectra of $CeRh_{1-x}Ir_xIn_5$ for several different values of x at 5 K. In ($I = 9/2$) has nine transitions for each site, and all transitions are split by the quadrupolar interaction [31]. The In sites were identified by fitting the spectra using the nuclear spin Hamiltonian:

$$\mathcal{H} = \gamma\hbar\mathbf{I}\cdot(1+\mathbf{K})\cdot\mathbf{H}_0 + \frac{h\nu_{zz}}{6}\left[3I_z^2 - \hat{I}^2 + \eta\left(\hat{I}_x^2 - I_y^2\right)\right], \tag{3}$$

where $\gamma = 0.93295$ kHz/G is the gyromagnetic ratio, I_α are the nuclear spin operators, $\mathbf{K}$ is the Knight shift tensor, ν_{zz} is the largest eigenvalue of the electric field gradient (EFG) tensor, and η is the asymmetry parameter. The (x, y, z) coordinates are defined in the usual manner such that $|\nu_{zz}| > |\nu_{xx}| > |\nu_{yy}|$. For In(1), z corresponds to the c axis, and for In(2), z corresponds to the direction normal to the unit cell face containing the In(2) atom, whereas x corresponds to the other in-plane direction perpendicular to c. The resonance frequencies of the In(1) depend on K, the field orientation, and ν_{cc}. The In(2) resonances are more complex due to the nonzero EFG asymmetry parameter, $\eta = |\nu_{xx}| - |\nu_{yy}|)/|\nu_{zz}|$, and misorientations from $\mathbf{H}_0 \,||\, c$ split the In(2) resonances, giving rise to double peaks. Furthermore, local disorder and

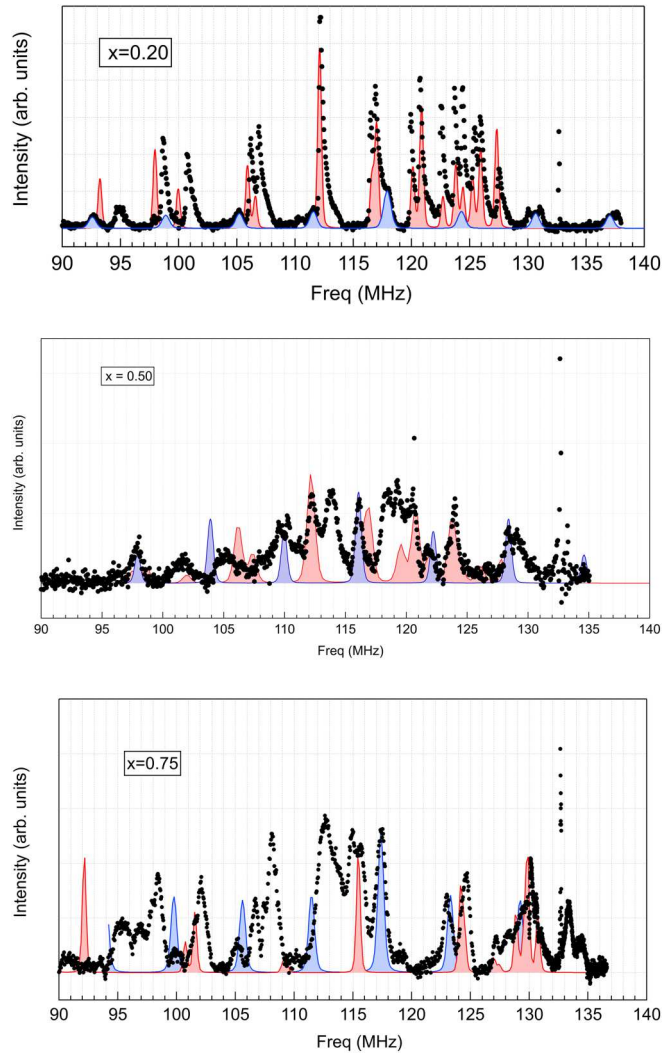

FIG. 3. NMR spectrum for $CeRh_{1-x}Ir_xIn_5$ with $x = 0.20$ (top), $x = 0.50$ (middle), and $x = 0.75$ (bottom). Fits to the In(1) sites are shown in blue, and those for the In(2) sites are shown in red. The fit parameters for $x = 0.20$ are $\theta = 4^\circ \pm 3^\circ$, $\phi = 8^\circ \pm 3^\circ$, $K_c(1) = 7.8\% \pm 0.1\%$, $K_c(2) = 2.5\% \pm 0.1\%$, $\nu_{zz}(1) = 6.41 \pm 0.5$ MHz, $\nu_{zz}(2) = 17.3 \pm 0.5$ MHz, and $\eta(2) = 0.45 \pm 0.02$. The fit parameters for $x = 0.50$ are $\theta = 8.3^\circ \pm 3^\circ$, $\phi = 11^\circ \pm 3^\circ$, $K_c(1) = 6.2\% \pm 0.2\%$, $K_c(2) = 2.8\% \pm 0.5\%$, $\nu_{zz}(1) = 6.32 \pm 0.2$ MHz, $\nu_{zz}(2) = 16.57 \pm 0.5$ MHz, and $\eta(2) = 0.45 \pm 0.02$. The fit parameters for $x = 0.75$ are $\theta = 6^\circ \pm 3^\circ$, $\phi = 0^\circ$, $K_c(1) = 7.3\% \pm 0.2\%$, $K_c(2) = 5.4\% \pm 0.8\%$, $\nu_{zz}(1) = 6.0$ MHz, $\nu_{zz}(2) = 17.28 \pm 0.5$ MHz, and $\eta(2) = 0.45 \pm 0.02$.

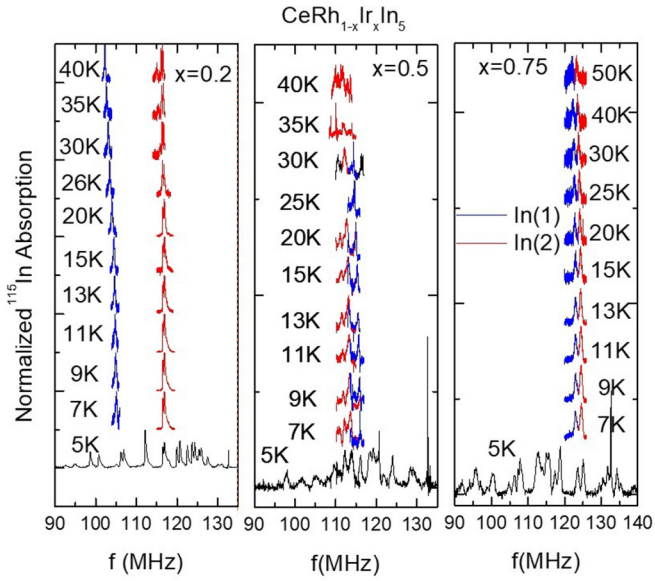

FIG. 4. Spectra of $CeRh_{1-x}Ir_xIn_5$ for $x = 0.20$, $x = 0.50$, and $x = 0.75$ for several different temperatures for $H_0 = 11.7$ T along the c direction. Blue indicates In(1), and red indicates In(2). Slight misalignments cause the In(2) spectra to split.

mixing of Rh and Ir in the substitutional samples are responsible for multiple In(2) sites and create complex NMR spectra.

To fit the spectra, we assume the direction of $\mathbf{H}_0$ is described by the spherical polar angles (θ, ϕ) with respect to the c axis and perform an exact diagonalization of Eq. (3). The peaks in Fig. 3 are fit to Voigt functions. The EFG values agree with previous measurements [35]. Although we are able to fit the full In(1) spectra, one peak at 104 MHz peak is not apparent in the experimental data for $x = 0.5$. The reason for this discrepancy is unclear but may be related to poor tuning conditions of the probe. There are also several peaks that are not fully identified, which are likely due to In(2) sites associated with local disorder due to the nonstoichiometry of Rh and Ir. Note that when $\theta \neq 0°$, the In(2) sites split into two peaks. Moreover, because In(2) has nonaxial symmetry, the resonance frequencies are strong functions of the relative orientation between $\mathbf{H}_0$ and the EFG tensor. Local disorder at an In(2) site can affect both the magnitude of the EFG tensor components and the orientation of the principle EFG axes. Nevertheless, these sites are not relevant for understanding the behavior of the hyperfine coupling, and we focus our analysis solely on the sites that have been clearly identified. Figure 4 shows the temperature dependence of specific well-defined resonances. There are clear shifts of the resonance frequencies with increasing temperature. We assume that the EFG remains temperature independent and that the temperature dependence arises solely from the Knight shift.

C. Knight shift

The Knight shift of In(1) K_1 is shown in Fig. 5 as a function of temperature and Ir substitution x for a field aligned along the c direction. K_1 decreases with x, similar to χ, although there are small deviations at low temperature. For

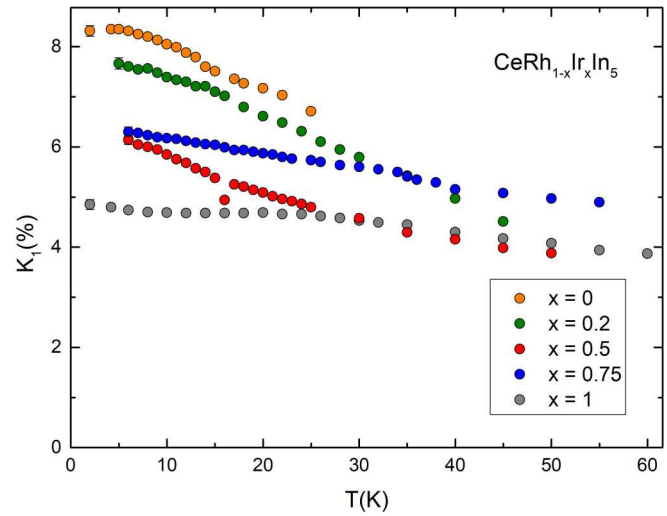

FIG. 5. In(1) Knight shift versus temperature. Data for $x = 0$ and $x = 1$ are reproduced from [28].

the hyperfine interaction in heavy fermions, the Knight shift is given by $K = A\chi_{cc} + (A + B)\chi_{cf} + B\chi_{ff}$, where χ_{cc}, χ_{ff}, and χ_{cf} are contributions from the conduction electrons, the f moments, and their interaction, respectively [25]. Here we write $B = nB_{cc}$, where n is the number of nearest-neighbor f sites [$n = 4$ for In(1) and 2 for In(2)] and B_{cc} corresponds to the c-axis component of the tensor $\mathbb{B}$. The total susceptibility is $\chi = \chi_{cc} + 2\chi_{cf} + \chi_{ff}$. For sufficiently high temperatures $T > T^*$ the first two contributions to the shift can be ignored, and $K \approx B\chi$. A plot of K_1 versus χ yields a straight line for $T > T^*$ with slope B_1, as shown in Fig. 6. Figure 7 shows the

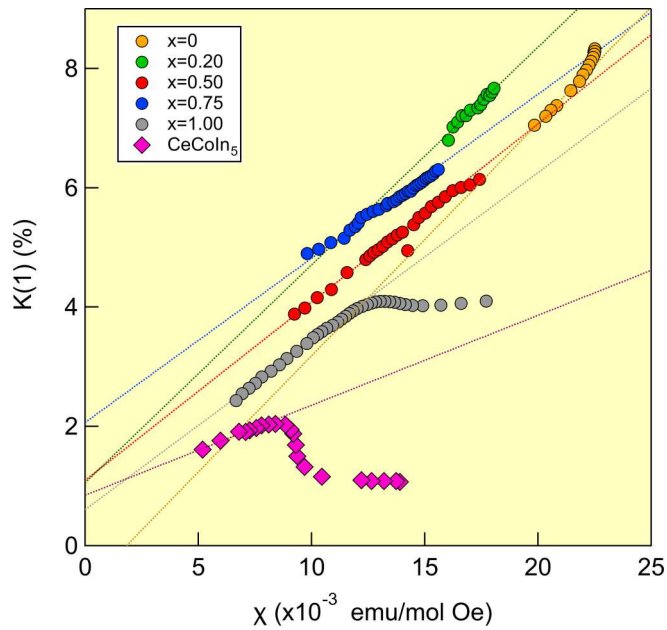

FIG. 6. In(1) Knight shift versus magnetic susceptibility. Dotted lines are fits to the high-temperature ($T > T^*$) data. Data for $CeCoIn_5$ are reproduced from [40]; data for $x = 0$ and $x = 1$ are reproduced from [28].

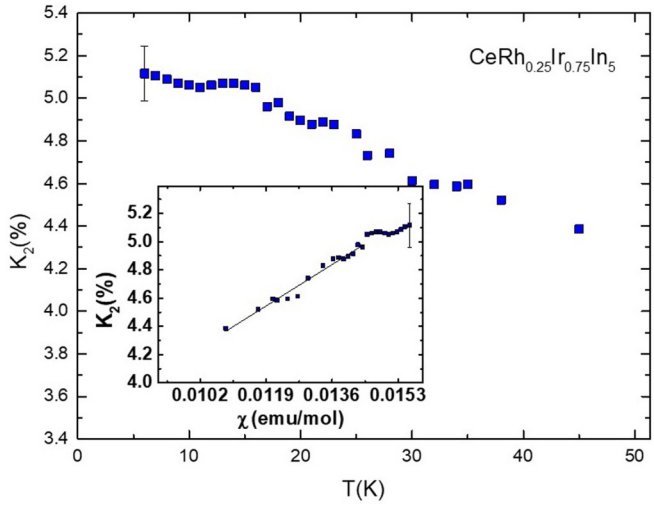

FIG. 7. In(2) Knight shift versus temperature for $x = 0.75$. The inset shows $K(2)$ versus χ, and the solid line is the best fit to the high-temperature data.

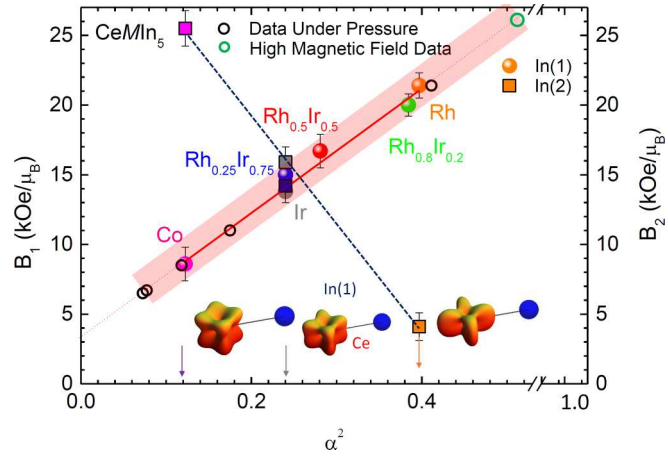

FIG. 8. The transferred hyperfine coupling to In(1) and In(2) as a function of α^2. The lines are fits to $B_{1,2}(\alpha^2) = B_{1,2}(0) + \kappa_{1,2}\alpha^2$, where $B_1(0) = 3.3(8)$ kOe/μ_B, $B_2(0) = 32(1)$ kOe/μ_B, $\kappa_1 = 44(2)$ kOe/μ_B, and $\kappa_2 = -59(2)$ kOe/μ_B. The open black circles represent $CeRhIn_5$ under pressure and are taken from Ref. [31] and infer the α^2 values using the fit to the ambient-pressure data (shown in Fig. 9). The open green circle represents $CeRhIn_5$ at high fields above 31 T, taken from Ref. [41]. The insets at the bottom show how the spatial form of the Ce $4f$ wave function evolves as α^2 changes.

Knight shift for In(2) for $x = 0.75$. We are unable to reliably extract the In(2) Knight shift for the other substitutions due to misalignments and spectral overlap with other sites.

There are two important trends evident in Fig. 6. First, the slope decreases with increasing x and gets even smaller in $CeCoIn_5$. Second, there is a breakdown in the linear relationship below a temperature T^*. This deviation signals the onset of coherence at low temperatures, where χ_{cc} and χ_{cf} can no longer be ignored. As x increases from 0 to 1, the deviation evolves from curving upwards (pure $CeRhIn_5$) to downwards (undoped $CeIrIn_5$) and becomes more pronounced for $CeCoIn_5$. For intermediate values of $x \approx 0.5$, there is no clear evidence of such a deviation in the data. This behavior reflects changes in the relative size of the on-site A coupling to the transferred B coupling, as well as the growth of heavy-fermion coherence, as discussed below.

IV. DISCUSSION

We can now examine how the hyperfine coupling correlates with the CEF ground state orbital shape. Figure 8 shows the B_1 and B_2 transferred hyperfine couplings to In(1) and In(2), respectively, versus α^2, using the parameters extracted from the fits to the Knight shift and susceptibility. The lines in Fig. 8 are linear fits to the data, including the value for $CeCoIn_5$ [40]. As α^2 increases, the orbitals become more oblate, the lobes pointing along the In(1) directions become more extended, and the transferred hyperfine coupling to the In(1) nucleus increases.

In order to understand this behavior quantitatively, we consider a simple model in which the transferred coupling is directly proportional to the magnitude squared of the Ce $4f$ wave function along the Ce-In(1) bond direction. The angular dependence of this probability is given by the function $f_\alpha(\theta, \phi) = \sum_{m_S} |\langle \theta, \phi, m_S | \psi(\Gamma_7^{(1)}) \rangle|^2$, shown as insets in Fig. 8 for various values of α. The wave function is given by Eq. (2), where

$$|J_z\rangle = \sum_{m'_L=-3}^{3} \sum_{m'_S=-1/2}^{1/2} C_{m'_L,m'_S;J_z} |L, m'_L\rangle |S, m'_S\rangle \qquad (4)$$

and $C_{m'_L,m'_S;J_z}$ are the appropriate Clebsch-Gordan coefficients for $L = 3$, $S = 1/2$, and $J = 5/2$. Along the Ce-In(1) bond direction $f_\alpha(\theta = \frac{\pi}{2}, \phi = \frac{\pi}{4}) \sim 1 + 4\alpha^2 + 2\sqrt{5\alpha^2(1-\alpha^2)}$. This function grows over the range $0.2 \lesssim \alpha^2 \lesssim 0.8$, in agreement with our observation that the hyperfine coupling increases with α^2.

Direct measurements of the In(2) hyperfine coupling are challenging in the doped materials. However, it is insightful to consider the values for pure $CeRhIn_5$, $CeIrIn_5$, and $CeCoIn_5$ versus α^2 [28], as well as for the $x = 0.75$ sample. In contrast to In(1), B_2 is largest when the orbital lobes extend out of the plane and decreases with increasing α^2. The exact value of θ to use for $f_\alpha(\theta, \phi)$ depends on the position of In(2) within the unit cell; however, it can be well approximated as $f_\alpha(\theta \approx \frac{3\pi}{4}, \phi = 0) \sim 51 - 6\alpha(6\alpha + \sqrt{5 - 5\alpha^2})$. This quantity decreases as α^2 increases, which again agrees with the behavior observed in Fig. 8. These results reveal directly how the hybridizations to the in-plane In(1) and out-of-plane In(2) sites evolve as the ground state orbital anisotropy changes.

Similar changes in the transferred hyperfine couplings were observed in $CeRhIn_5$ under hydrostatic pressure [31]. In this case, B_1 decreases from 25.6 to 5.2 kOe/μ_B between ambient pressure and ~2 GPa, which is close to the value observed in pure $CeCoIn_5$. Using the linear relationship between B_1 and α^2 we observe under ambient pressure in Fig. 8, we infer the pressure dependence of α^2 in Fig. 9(a). These results imply that pressure changes the CEF parameters so that the Ce $4f$ wave function lobes extend more out of the plane,

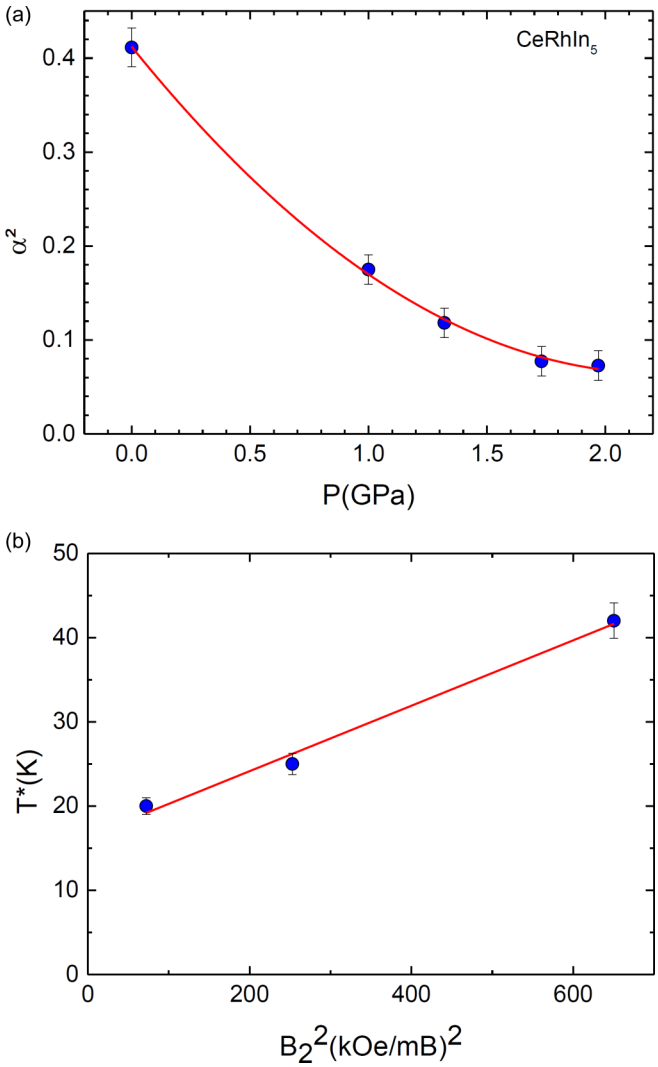

FIG. 9. (a) α^2 inferred from the pressure dependence of B_1 in [31] using the relationship measured at ambient pressure in Fig. 8. The solid line is a guide to the eye. (b) The coherence temperature T^* versus B_2^2. The solid line is given by $T^* = 16.3(2) + 0.039(3)B_2^2$.

becoming more cubiclike. This observation is consistent with the fact that at this pressure, $CeRhIn_5$ becomes superconducting with T_c similar to $CeCoIn_5$ and develops a large Fermi surface [17,36]. On the other hand, the data imply that α^2 becomes smaller than $\alpha_c = 1/6$, which may be unphysical. It should be noted, however, that the values for B_1 in [31] were determined based on the assumption that the In(2) hyperfine coupling did not change under pressure. Because there are no independent susceptibility data under pressure, it was only possible to directly extract the ratio of $B_1(P)$ to $B_2(P)$, rather than their independent values. Nevertheless, the trend under hydrostatic pressure is similar to that observed with chemical pressure. A possible explanation for the behavior of the In(2) hyperfine coupling is that under pressure the wave function acquires an admixture of the $\Gamma_7^{(2)}$ excited states due to the Kondo coupling, similar to recent observations in $CeCoIn_5$ [42]. Because the $\Gamma_7^{(2)}$ state is rotated 45° relative to the $\Gamma_7^{(1)}$ state, any admixture would dramatically affect the hyperfine couplings B_1 and possibly B_2. Future measurements of the In(2) Knight shift for in-plane fields in $CeRhIn_5$ will be necessary to check this scenario.

The Knight shift anomaly observed in Fig. 6 reflects the growth of $K_{HF}(T)$ below T^*, where $K_{HF}(T) \propto (A - B)(1 - T/T^*)^{3/2}[1 + \ln(T^*/T)]$ [28]. As B_1 increases with α^2, the sign of $K_{HF}(T)$ changes from positive to negative and vanishes when the transferred coupling equals the on-site coupling A. Previously, $A \approx 14$ kOe/μ_B was estimated in $CeCoIn_5$ [29]. Since this quantity reflects a combination of a Fermi-contact interaction plus core polarization from the indium $5p$ orbitals, it should only weakly depend on doping or transition metal element. Thus, the observation that the Knight shift anomaly is small or absent in $CeRh_{1-x}Ir_xIn_5$ for $x \approx 0.5$ in Fig. 6 likely reflects the fact that $B_1 \approx A$ in this range. On the other hand, there is clear growth of both the magnitude of K_{HF} and the onset temperature T^* as α^2 decreases in $CeIrIn_5$ and $CeCoIn_5$. T^* is approximately the temperature where the entropy reaches $R \ln 2$ and has been shown to be empirically related to the Kondo coupling J as $T^* = 0.45J^2\rho$, where ρ is the density of conduction electron states [19]. Since the Kondo coupling arises due to hybridization of the $4f$ orbital, it is natural to expect that $J \propto \alpha^2$, and thus $T^* \sim B_2^2$, as demonstrated in Fig. 9(b). This observation supports previous dynamical mean-field theory calculations of $CeIrIn_5$ that indicated the hybridization gap for the Ce-In(2) band dominates that for the in-plane Ce-In(1) band [12]. The Kondo hybridization, which drives the low-temperature correlated behavior, is thus directly controlled by the shape of the Ce $4f$ orbitals.

V. SUMMARY

We have measured the Knight shift and magnetic susceptibilities for several single crystals of $CeRh_{1-x}Ir_xIn_5$ and have found that the transferred hyperfine couplings to In(1) and In(2) vary linearly with α^2, where α describes the admixture between the $|J_z = -\frac{3}{2}\rangle$ and $|J_z = +\frac{5}{2}\rangle$ states of the Ce $4f$ ground state wave function. The hyperfine coupling to In(1) is enhanced as α^2 grows and the wave function extends out of the plane. The coupling to In(2), on the other hand, decreases as α^2 increases. These results provide direct proof that the hybridization between the $4f$ wave function and the In $5p$ orbitals is controlled by the orbital anisotropy. This observation also offers an explanation for the abrupt decrease in the In(1) Knight shift at 30 T, where the magnetic field induces changes in the crystal field ground state orbital [41], and for the pressure dependence of the coupling to In(1). A detail that has not been considered in our analysis is that it is possible that the Kondo coupling to the excited state $\Gamma_7^{(2)}$ manifold alters the shape of the $4f$ orbital, which may play a role in the pressure dependence of the ratio B_1/B_2 under pressure [31]. Further experiments exploring all components of the hyperfine coupling tensor will be important to better characterize this hybridization, especially under pressure. This study establishes transferred hyperfine interactions as an important probe of hybridization anisotropy in heavy-fermion materials, and may provide a more straightforward approach to determine the crystal field parameters.

ACKNOWLEDGMENTS

The authors gratefully acknowledge support from the UC Davis Seed Grant program and FAPESP (Grants No. gg2016/14436-3, No. 2020/12283-0, No. 2018/11364-7, No. 2017/10581-1, and No. 2012/05903-6). R.R.U. acknowledges CNPq Grant No. 309483/2018-2. P.G.P. acknowledges CNPq Grant No. 304496/2017-0. We acknowledge helpful discussions with T. Kissikov and P. Klavins. Work at UC Davis was partially supported by the NSF under Grant No. DMR-1807889.

[1] S. Doniach, The Kondo lattice and weak antiferromagnetism, Physica B+C (Amsterdam) **91**, 231 (1977).

[2] Z. Fisk, D. W. Hess, C. J. Pethick, D. Pines, J. L. Smith, J. D. Thompson, and J. O. Willis, Heavy-electron metals: New highly correlated states of matter, Science **239**, 33 (1988).

[3] G. R. Stewart, Non-Fermi-liquid behavior in d- and f-electron metals, Rev. Mod. Phys. **73**, 797 (2001).

[4] P. Coleman and A. J. Schofield, Quantum criticality, Nature (London) **433**, 226 (2005).

[5] Q. M. Si, S. Rabello, K. Ingersent, and J. L. Smith, Locally critical quantum phase transitions in strongly correlated metals, Nature (London) **413**, 804 (2001).

[6] J. Custers, P. Gegenwart, H. Wilhelm, K. Neumaier, Y. Tokiwa, O. Trovarelli, C. Geibel, F. Steglich, C. Pepin, and P. Coleman, The break-up of heavy electrons at a quantum critical point, Nature (London) **424**, 524 (2003).

[7] P. Gegenwart, Q. Si, and F. Steglich, Quantum criticality in heavy-fermion metals, Nat. Phys. **4**, 186 (2008).

[8] J. R. Schrieffer and P. A. Wolff, Relation between the Anderson and Kondo Hamiltonians, Phys. Rev. **149**, 491 (1966).

[9] M. Vekic, J. W. Cannon, D. J. Scalapino, R. T. Scalettar, and R. L. Sugar, Competition between Antiferromagnetic Order and Spin-Liquid Behavior in the Two-Dimensional Periodic Anderson Model at Half Filling, Phys Rev. Lett. **74**, 2367(R) (1995).

[10] M. Jiang, N. J. Curro, and R. T. Scalettar, Universal Knight shift anomaly in the periodic Anderson model, Phys. Rev. B **90**, 241109(R) (2014).

[11] N. C. Costa, T. Mendes-Santos, T. Paiva, N. J. Curro, R. R. dos Santos, and R. T. Scalettar, Coherence temperature in the diluted periodic Anderson model, Phys. Rev. B **99**, 195116 (2019).

[12] J. Shim, K. Haule, and G. Kotliar, Modeling the localized-to-itinerant electronic transition in the heavy fermion system $CeIrIn_5$, Science **318**, 1615 (2007).

[13] K. S. Burch, S. V. Dordevic, F. P. Mena, A. B. Kuzmenko, D. van der Marel, J. L. Sarrao, J. R. Jeffries, E. D. Bauer, M. B. Maple, and D. N. Basov, Optical signatures of momentum-dependent hybridization of the local moments and conduction electrons in Kondo lattices, Phys. Rev. B **75**, 054523 (2007).

[14] T. Willers, F. Strigari, Z. Hu, V. Sessi, N. B. Brookes, E. D. Bauer, J. L. Sarrao, J. D. Thompson, A. Tanaka, S. Wirth, L. H. Tjeng, and A. Severing, Correlation between ground state and orbital anisotropy in heavy fermion materials, Proc. Natl. Acad. Sci. USA **112**, 2384 (2015).

[15] A. C. Shockley, K. R. Shirer, J. Crocker, A. P. Dioguardi, C. H. Lin, D. M. Nisson, N. apRoberts-Warren, P. Klavins, and N. J. Curro, NMR evidence of anisotropic Kondo liquid behavior in $CeIrIn_5$, Phys. Rev. B **92**, 085108 (2015).

[16] J. Thompson, R. Movshovich, Z. Fisk, F. Bouquet, N. Curro, R. Fisher, P. Hammel, H. Hegger, M. Hundley, M. Jaime, P. Pagliuso, C. Petrovic, N. Phillips, and J. Sarrao, Superconductivity and magnetism in a new class of heavy-fermion materials, J. Magn. Magn. Mater. **226**, 5 (2001).

[17] T. Park, F. Ronning, H. Q. Yuan, M. B. Salamon, R. Movshovich, J. L. Sarrao, and J. D. Thompson, Hidden magnetism and quantum criticality in the heavy fermion superconductor $CeRhIn_5$, Nature (London) **440**, 65 (2006).

[18] T. Park, V. A. Sidorov, F. Ronning, J.-X. Zhu, Y. Tokiwa, H. Lee, E. D. Bauer, R. Movshovich, J. L. Sarrao, and J. D. Thompson, Isotropic quantum scattering and unconventional superconductivity, Nature (London) **456**, 366 (2008).

[19] Y.-F. Yang, Z. Fisk, H.-O. Lee, J. D. Thompson, and D. Pines, Scaling the Kondo lattice, Nature (London) **454**, 611 (2008).

[20] J. L. Sarrao, L. A. Morales, J. D. Thompson, B. L. Scott, G. R. Stewart, F. Wastin, J. Rebizant, P. Boulet, E. Colineau, and G. H. Lander, Plutonium-based superconductivity with a transition temperature above 18 K, Nature (London) **420**, 297 (2002).

[21] F. Wastin, P. Boulet, J. Rebizant, E. Colineau, and G. H. Lander, Advances in the preparation and characterization of transuranium systems, J. Phys.: Condens. Matter **15**, S2279 (2003).

[22] N. Curro, T. Caldwell, E. Bauer, L. Morales, M. Graf, Y. Bang, A. Balatsky, J. Thompson, and J. Sarrao, Unconventional superconductivity in $PuCoGa_5$, Nature (London) **434**, 622 (2005).

[23] P. Pagliuso, R. Movshovich, A. Bianchi, M. Nicklas, N. Moreno, J. Thompson, M. Hundley, J. Sarrao, and Z. Fisk, Multiple phase transitions in Ce(Rh, Ir, Co)In_5, Phys. B (Amsterdam, Neth.) **312–313**, 129 (2002).

[24] E. D. Bauer, J. D. Thompson, J. L. Sarrao, L. A. Morales, F. Wastin, J. Rebizant, J. C. Griveau, P. Javorsky, P. Boulet, E. Colineau, G. H. Lander, and G. R. Stewart, Structural Tuning of Unconventional Superconductivity in PuMGa$_5$ (M = Co,Rh), Phys. Rev. Lett. **93**, 147005 (2004).

[25] N. J. Curro, Hyperfine interactions in the heavy fermion $CeMIn_5$ systems, New J. Phys. **8**, 173 (2006).

[26] N. J. Curro, B.-L. Young, R. R. Urbano, and M. J. Graf, Hyperfine fields and magnetic structure in the B phase of $CeCoIn_5$, J. Low Temp. Phys. **158**, 635 (2010).

[27] S. Renold, S. Pliberšek, E. Stoll, T. Claxton, and P. Meier, First-principles calculation of electric field gradients and hyperfine couplings in $YBa_2Cu_3O_7$, Eur. Phys. J. B **23**, 3 (2001).

[28] K. R. Shirer, A. C. Shockley, A. P. Dioguardi, J. Crocker, C. H. Lin, N. apRoberts Warren, D. M. Nisson, P. Klavins, J. C. Cooley, Y.-f. Yang, and N. J. Curro, Long range order and two-fluid behavior in heavy electron materials, Proc. Natl. Acad. Sci. USA **109**, E3067 (2012).

[29] N. J. Curro, B. L. Young, J. Schmalian, and D. Pines, Scaling in the emergent behavior of heavy-electron materials, Phys. Rev. B **70**, 235117 (2004).

[30] S. Kambe, Y. Tokunaga, H. Sakai, H. Chudo, Y. Haga, T. D. Matsuda, and R. E. Walstedt, One-component description of magnetic excitations in the heavy-fermion compound $CeIrIn_5$, Phys. Rev. B **81**, 140405(R) (2010).

[31] C. H. Lin, K. R. Shirer, J. Crocker, A. P. Dioguardi, M. M. Lawson, B. T. Bush, P. Klavins, and N. J. Curro, Evolution of hyperfine parameters across a quantum critical point in $CeRhIn_5$, Phys. Rev. B **92**, 155147 (2015).

[32] C. Petrovic, R. Movshovich, M. Jaime, P. G. Pagliuso, M. F. Hundley, J. L. Sarrao, Z. Fisk, and J. D. Thompson, A new heavy-fermion superconductor $CeIrIn_5$: A relative of the cuprates? Europhys. Lett. **53**, 354 (2001).

[33] P. G. Pagliuso, C. Petrovic, R. Movshovich, D. Hall, M. F. Hundley, J. L. Sarrao, J. D. Thompson, and Z. Fisk, Coexistence of magnetism and superconductivity in $CeRh_{1-x}Ir_xIn_5$, Phys. Rev. B **64**, 100503(R) (2001).

[34] P. G. Pagliuso, D. J. Garcia, E. Miranda, E. Granado, R. Lora Serrano, C. Giles, J. G. S. Duque, R. R. Urbano, C. Rettori, J. D. Thompson, M. F. Hundley, and J. L. Sarrao, Evolution of the magnetic properties and magnetic structures along the R_mMIn_{3m+2} (R=Ce, Nd, Gd, Tb; M=Rh, Ir; and $m = 1, 2$) series of intermetallic compounds, J. Appl. Phys. **99**, 08P703 (2006).

[35] S. Kawasaki, M. Yashima, Y. Mugino, H. Mukuda, Y. Kitaoka, H. Shishido, and Y. Ōnuki, Enhancing the Superconducting Transition Temperature of $CeRh_{1-x}Ir_xIn_5$ Due to the Strong-Coupling Effects of Antiferromagnetic Spin Fluctuations: An ^{115}In Nuclear Quadrupole Resonance Study, Phys. Rev. Lett. **96**, 147001 (2006).

[36] H. Shishido, R. Settai, H. Harima, and Y. Ōnuki, A drastic change of the Fermi surface at a critical pressure in $CeRhIn_5$: dHvA study under pressure, J. Phys. Soc. Jpn. **74**, 1103 (2005).

[37] Y. Haga, Y. Inada, H. Harima, K. Oikawa, M. Murakawa, H. Nakawaki, Y. Tokiwa, D. Aoki, H. Shishido, S. Ikeda, N. Watanabe, and Y. Ōnuki, Quasi-two-dimensional Fermi surfaces of the heavy fermion superconductor $CeIrIn_5$, Phys. Rev. B **63**, 060503(R) (2001).

[38] K. Haule, Quantum Monte Carlo impurity solver for cluster dynamical mean-field theory and electronic structure calculations with adjustable cluster base, Phys. Rev. B **75**, 155113 (2007).

[39] T. Willers, Z. Hu, N. Hollmann, P. O. Körner, J. Gegner, T. Burnus, H. Fujiwara, A. Tanaka, D. Schmitz, H. H. Hsieh, H.-J. Lin, C. T. Chen, E. D. Bauer, J. L. Sarrao, E. Goremychkin, M. Koza, L. H. Tjeng, and A. Severing, Crystal-field and Kondo-scale investigations of $CeMIn_5$ (M = Co, Ir, and Rh): A combined x-ray absorption and inelastic neutron scattering study, Phys. Rev. B **81**, 195114 (2010).

[40] N. J. Curro, B. Simovic, P. C. Hammel, P. G. Pagliuso, J. L. Sarrao, J. D. Thompson, and G. B. Martins, Anomalous NMR magnetic shifts in $CeCoIn_5$, Phys. Rev. B **64**, 180514(R) (2001).

[41] G. G. Lesseux, H. Sakai, T. Hattori, Y. Tokunaga, S. Kambe, P. L. Kuhns, A. P. Reyes, J. D. Thompson, P. G. Pagliuso, and R. R. Urbano, Orbitally defined field-induced electronic state in a Kondo lattice, Phys. Rev. B **101**, 165111 (2020).

[42] M. Sundermann, A. Amorese, F. Strigari, B. Leedahl, L. H. Tjeng, M. W. Haverkort, H. Gretarsson, H. Yavaş, M. M. Sala, E. D. Bauer, P. F. S. Rosa, J. D. Thompson, and A. Severing, Orientation of the ground-state orbital in $CeCoIn_5$ and $CeRhIn_5$, Phys. Rev. B **99**, 235143 (2019).